Journal of Intelligent Material Systems and Structures

*Original Article*

*Journal of Intelligent Material Systems and Structures*
2015, Vol. 26(15) 1995–2010

DOI: 10.1177/1045389X14546652
jim.sagepub.com
SAGE

# Dynamic analysis and $\mathcal{H}_2$ optimisation of a piezo-based tuned vibration absorber

**Guoying Zhao[1], Neven Alujević[1], Bruno Depraetere[2] and Paul Sas[1]**

**Abstract**

In this article, a piezo-based tuned vibration absorber is proposed and theoretically analysed. The proposed device consists of a proof mass, a piezoelectric actuator and a resilient element (spring). An equivalent mechanical model where the piezoelectric element is connected to a general circuit composed of a resistor, an inductor and a capacitor in series (*RLC*) is presented to illustrate the coupling of the electrical components with the mechanical systems. Based on the mechanical replacement model, a *C* or *L* circuit can be used to realise a piezo-based tuned vibration neutraliser, while with an *RC* or *RL* circuit the piezo-based tuned vibration absorber can be considered as a piezo-based tuned mass damper. For the *C* and *L* circuits, tuning strategies are derived to adjust the shunt capacitance and inductance to track the disturbance frequency. In the case of *RC* and *RL* shunt circuits, an $\mathcal{H}_2$ optimisation criterion is used for tuning the piezo-based tuned mass damper. Closed-form expressions for the optimal tuning parameters are provided in this article.

**Keywords**

Piezoelectric element, tuned vibration absorber, shunt circuit, $\mathcal{H}_2$ optimisation

## Introduction

Dynamic vibration absorbers (DVAs) have been widely used to suppress undesirable vibrations of various types of mechanical structures such as machinery, helicopters, bridges and buildings. The most generic form of a DVA is an auxiliary system that consists of a mass and a spring or a spring–dashpot pair. Depending on whether the excitation of the primary structure is at a specific single frequency or it covers a broad range of frequencies, the design requirements on DVAs are different. When the primary system is subjected to a harmonic excitation, the DVA can be carefully designed such that its resonance frequency coincides with the excitation frequency. If the absorber damping is small, the DVA will significantly suppress vibrations over a very narrow bandwidth around the resonance frequency of the DVA (Den Hartog, 1934; Hunt, 1979; Mead, 1999). This type of absorber is often referred to as vibration neutraliser.

On the other hand, if the disturbance has a broad frequency range, which occurs, for example, with aerodynamic loading, vehicle road excitations, earthquakes or impacts, achieving reductions at a single frequency is not necessarily useful, but reduction in a given frequency band is required. In such cases, the damping of the absorber should be increased so that certain vibration metrics are minimised in the frequency band of interest (Warburton, 1982). This type of absorber is often referred to as tuned mass damper (TMD).

For both types of DVA, deviation from the desired settings can seriously degrade the performance (Von Flotow et al., 1994). For example, a mistuned vibration neutraliser could actually amplify the vibration of its host structure due to a drift in the excitation frequency. Similarly, a mistuned mass damper yields less vibration reduction of the host structure in the interesting frequency band. As a result, DVAs with tuneable properties have been extensively studied. For example, the resonance frequency of a DVA can be tuned through changing the stiffness of the absorber spring. In this case, variable geometries or active smart materials can be used to realise the absorber spring. Examples of former can be found in Walsh and Lamancusa (1992), Kidner and Brennan (2001) and Bonello et al. (2005); however, it is quite a design challenge to develop a

[1]Production Engineering, Machine Design and Automation (PMA) Section, KU Leuven, Heverlee, Belgium
[2]Flanders' Mechatronics Technology Centre (FMTC), Heverlee, Belgium

**Corresponding author:**
Guoying Zhao, Production Engineering, Machine Design and Automation (PMA) Section, KU Leuven, Celestijnenlaan 300b – Box 2420, 3001 Heverlee, Leuven, Belgium.
Email: guoying.zhao@mech.kuleuven.be

practical and rugged adaptive device under the constraints of weight, size and cost (Sun et al., 1995). Therefore, the realisation of a tuneable DVA using smart materials (active elements) has recently drawn a lot of attention (Alujević et al., 2012; Gardonio and Zilletti, 2013; Jalili and Fallahi, 2002; Rustighi et al., 2005; Williams et al., 2002). In most cases, the active elements are placed in parallel with the resilient element, which support the reaction mass. With appropriate control algorithms to regulate the input voltage or current, a smart material-based vibration absorber is able to track the variation in a tonal excitation frequency (Hollkamp and Starchville, 1994; Niederberger, 2005) or minimise vibrations of the host structure in a frequency band of interest (Behrens et al., 2003; Neubauer et al., 2006).

Because of their relatively high electromechanical transduction properties (Moheimani and Fleming, 2006), piezoelectric materials offer an attractive possibility for implementing tuneable vibration absorbers. The principle is that a change in the electrical boundary conditions of the piezoelectric element leads to a change in its mechanical properties such as its effective stiffness and effective damping (Date et al., 2000; Lesieutre, 1998). If part of the vibration absorber stiffness and damping is provided by the piezoelectric element, the properties of this vibration absorber can then in principle be controlled by a tuneable external electrical circuit connected to the piezoelectric element. Date et al. (2000) proved that the effective elastic modulus and the effective damping of polyvinylidene difluoride (PVDF) samples can be modified by connecting a negative capacitance and a resistance, respectively. Davis and Lesieutre (2000) developed a tuneable solid-state piezoelectric vibration absorber, where a piezoelectric transducer is incorporated into the suspension of a passive absorber. The resonance frequency of the developed device is thus partly determined by the stiffness of the piezoelectric element. By altering the positive switching shunt capacitance, a $\pm 3.7\%$ tuneable frequency band is reported.

An alternative *RL* circuit has also been investigated for realising shunt tuned DVAs (Hagood and Von Flotow, 1991; Hollkamp, 1994; Neubauer et al., 2006; Park and Inman, 2003; Sales et al., 2013; Wu, 1996). In these articles, the shunt circuit consisting of a resistor and inductor either in series or in parallel is discussed. The shunt inductance and resistance behave as an additional mass and damper, respectively, so that the shunted piezoelectric device acts as a damped vibration absorber. Apart from the above-mentioned linear shunt circuits, the switched shunts as nonlinear shunt circuits have also been studied (Corr and Clark, 2001; Guyomar et al., 2008). The principle is to continuously change the shunt impedance synchronously with the mechanical oscillations. In order to deal with the nonlinear behaviour of the switching shunt circuits, the harmonic balance method can be used to simplify the modelling of the nonlinear system (Neubauer and Wallaschek, 2010).

This article focuses on a systematic comparison of the performance of a piezo-based tuned vibration absorber (PBTVA) with different linear shunt circuits. An equivalent mechanical model for a PBTVA connected with a *RLC* circuit is presented. In particular, realisation of the piezo-based tuned vibration neutraliser (TVN) and the piezo-based TMD is addressed. The optimal shunt parameters are derived in closed-form formulations for the two cases. For a piezo-based TVN, the optimal shunt parameters are chosen such that the response of the primary structure at the exciting harmonic frequency is as small as possible. For the piezo-based TMD on the other hand, the optimal parameters are derived to minimise the kinetic energy of the primary mass in a given frequency band using an $\mathcal{H}_2$ optimisation scheme on the coupled system composed by the PBTVA and the primary structure. Depending on the mechanical properties of the primary structure and the PBTVA, a negative capacitance might be required, which can cause stability problems. A stability analysis is performed and the gain margin towards the stability boundary is determined. The principal contributions of the work presented are as follows: (a) the development of equivalent mechanical models that enable a straightforward interpretation of the physics behind the various shunt techniques, (b) the derivation of the optimal shunt parameters using an $\mathcal{H}_2$ optimisation criterion in the closed form (minimisation of the kinetic energy of the primary structure) and (c) the relative stability analysis based on the gain margin for the case when an active shunt circuit with 'negative capacitance' is employed.

This article is structured into five sections. In section 'Dynamic analysis of a piezo-based vibration absorber', the motion equations of the PBTVA system are derived. Based on these general equations, equivalent mechanical models for single *R*, *C* and *L* circuits are deduced. Sections 'Realisation of a piezo-based TVN' and 'Realisation of a piezo-based TMD' deal with the realisation of the piezo-based TVN and the piezo-based TMD, respectively. Closed-form expressions for the optimal shunt parameters are derived and their performance is compared. Section 'Conclusion' summarises the main conclusions of this article.

## Dynamic analysis of a piezo-based vibration absorber

The system under investigation is shown in Figure 1. The primary structure is modelled as a lumped parameter single-degree-of-freedom system ($m_1$, $k_1$ and $d_1$). The PBTVA consists of a reaction mass $m_2$, a damper $d_2$, a stiffness $k_2$ and a piezoelectric transducer. The

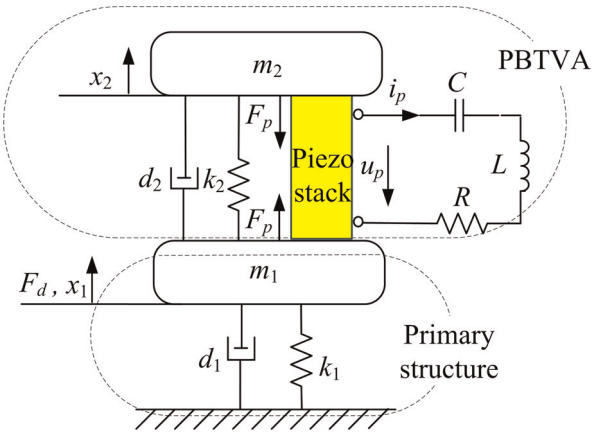


**Figure 1.** Scheme of the system under investigation.
PBTVA: piezo-based tuned vibration absorber.

stiffness $k_2$ represents all stiffness elements between masses $m_1$ and $m_2$, with the exception of the stiffness of the piezoelectric element.

The global constitutive equations of the piezoelectric element can be expressed as (Preumont, 2002)

$$Q_p = C_p(1-k^2)u_p + d_{33}k_m x \tag{1}$$

$$F_p = -d_{33}k_m u_p + k_m x \tag{2}$$

where $Q_p$ is the electric charge on the electrodes of the piezoelectric element, $x = x_2 - x_1$ is the extension of the piezoelectric stack; $F_p$ is the force acting on the surface of the piezoelectric element; $u_p$ is the voltage between the electrodes of the piezo; $C_p$ is the capacitance of the piezo with no external load ($F_p = 0$); $k_m$ is the stiffness of the piezoelectric element when its electrodes are short-circuited ($u_p = 0$); $k$ is the electromechanical coupling factor of the material, which gives the conversion efficiency of mechanical into electrical energy and vice versa and finally $d_{33}$ is the piezoelectric constant (m/V). Subscript 33 indicates that only the longitudinal direction of the piezoelectric element is considered and the electric field is parallel to the poling direction.

Considering a *RLC* serial shunt circuit is connected to the piezoelectric element, the relationship between the voltage $u_p$ over the piezoelectric element and its stroke $x$ can be established

$$LC_{ps}\ddot{u}_p + Ld_{33}k_m\ddot{x} + RC_{ps}\dot{u}_p + Rd_{33}k_m\dot{x} + \left(\frac{C_{ps}}{C} + 1\right)u_p + \frac{d_{33}k_m}{C}x = 0 \tag{3a}$$

where

$$C_{ps} = C_p(1-k^2) \tag{3b}$$

In equation (3a), $C$ can be positive or negative. A negative value indicates a negative capacitance, which can be emulated in practice using the circuit described in Date et al. (2000). In this article, the design of such a negative capacitance circuit is not addressed; an ideal negative capacitance is assumed throughout the study.

The equations of motion for the mechanical part of the system read

$$m_1\ddot{x}_1 + d_1\dot{x}_1 + d_2(\dot{x}_1 - \dot{x}_2) + k_1x_1 + k_2(x_1 - x_2) - F_p = F_d \tag{4}$$

$$m_2\ddot{x}_2 - d_2(\dot{x}_1 - \dot{x}_2) - k_2(x_1 - x_2) + F_p = 0 \tag{5}$$

where $F_p$ is the reaction force generated by the piezoelectric element as given in equation (2) and $F_d$ is the disturbance force.

In order to develop a fully mechanical replacement model, the voltage $u_p$ across the electrodes of the piezoelectric element and its stroke $x$ are grouped as $x_3$

$$x_3 = x_2 - x_1 + u_p\frac{C_{ps}}{d_{33}k_m} \tag{6}$$

Having the displacement $x_1$, $x_2$ and $x_3$ as the degree of freedom, the dynamic behaviour of the system is then described as

$$\begin{bmatrix} m_1 & 0 & 0 \\ 0 & m_2 & 0 \\ 0 & 0 & m_3 \end{bmatrix}\begin{bmatrix} \ddot{x}_1 \\ \ddot{x}_2 \\ \ddot{x}_3 \end{bmatrix} + \begin{bmatrix} d_1 + d_2 & -d_2 & 0 \\ -d_2 & d_2 & 0 \\ 0 & 0 & d_3 \end{bmatrix}\begin{bmatrix} \dot{x}_1 \\ \dot{x}_2 \\ \dot{x}_3 \end{bmatrix} + \begin{bmatrix} k_1 + k_2 + k_m + k_e & -k_2 - k_m - k_e & k_e \\ -k_2 - k_m - k_e & k_2 + k_m + k_e & -k_e \\ k_e & -k_e & k_e + k_c \end{bmatrix}\begin{bmatrix} x_1 \\ x_2 \\ x_3 \end{bmatrix} = \begin{bmatrix} F_s \\ 0 \\ 0 \end{bmatrix} \tag{7a}$$

with

$$m_3 = Lk^2k_mC_p \tag{7b}$$

$$d_3 = Rk^2k_mC_p \tag{7c}$$

$$k_c = k^2k_mC_p/C \tag{7d}$$

and

$$k_e = k^2k_mC_p/C_{ps} \tag{7e}$$

Using these notations, the inductance $L$, capacitance $C$, resistance $R$ and the piezoelectric capacitance $C_{ps}$ are represented by the equivalent mechanical mass $m_3$, damping $d_3$, spring $k_c$ and spring $k_e$, respectively. The third degree of freedom is the displacement of the equivalent mass $m_3$. Now, the reaction force $F_p$ produced by the piezoelectric element can be expressed only in terms of the mechanical parameters of the system

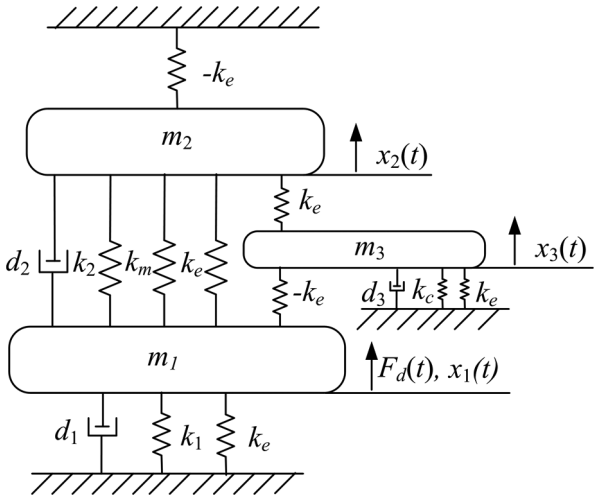


**Figure 2.** Mechanical replacement model for a general *RLC* circuit.

$$F_p = k_m(x_1 - x_2) + k_e(x_3 - x_2 + x_1) \tag{8}$$

As such, an equivalent mechanical model is developed with an identical dynamical behaviour as the system shown in Figure 1. This mechanical model is depicted in Figure 2; the first term of the right-hand side of equation (8) is described by spring $k_m$ between $m_2$ and $m_1$, while mass $m_3$, spring $k_c$, spring $k_e$ and the damping $d_3$ represent equation (8) and the right-hand side of equation (7a).

If damper $d_3$ and mass $m_3$ are absent ($R = 0$ and $L = 0$, respectively), the system shunt with only a capacitance can be considered. The corresponding equivalent model is shown in Figure 3(a), which can be further simplified to the model presented in Figure 3(b).

In Appendix 2, the equivalence of the two models shown in Figure 3 is presented. From the simplified model, it can be seen that the $C$ circuit is modelled as a spring $k_c$, which is added in series with the equivalent spring $k_e$ introduced by the piezoelectric capacitance. The case where $k_c = 0$ ($C = \infty$), corresponding to the short-circuited piezo, the branch that contains $k_c$ breaks such that no transmission force passes this branch and the piezoelectric effect disappears. In the open-circuit case where $k_c = \infty$ and consequently $C = 0$, there is no relative displacement over $k_c$ such that $k_e$ represents the whole branch.

Using a similar procedure, the equivalent mechanical model and its simplified model for the $R$ shunt circuit are presented in Figure 4(a) and (b). In the simplified model, the $R$ circuit is mapped to a damper, which is also placed in series with the equivalent spring $k_e$.

Finally, the equivalent mechanical model for the $L$ circuit can be obtained by removing spring $k_c$ and damper $d_3$, both shown in Figure 2. Then the shunt inductance is projected to an equivalent mass $m_3$ placed between masses $m_1$ and $m_2$ with a positive and a negative spring $k_e$, respectively.

In order to come to a more general formulation, the following non-dimensional parameters are introduced

$$\tau = \omega_1 t, \quad \mu = \frac{m_2}{m_1}, \quad f = \frac{\omega_2}{\omega_1}, \quad 2D_1 = \frac{d_1}{\omega_1 m_1},$$

$$2D_2 = \frac{d_2}{\omega_2 m_2}$$

$$2D_3 = C_{ps}\omega_1 R, \quad \lambda = C_{ps} L {\omega_1}^2,$$

$$\delta = \frac{C_{ps}}{C}, \quad \gamma = \frac{k_m k^2}{k_1(1-k^2)}, \quad \dot{x} = \omega_1 x' \tag{9}$$

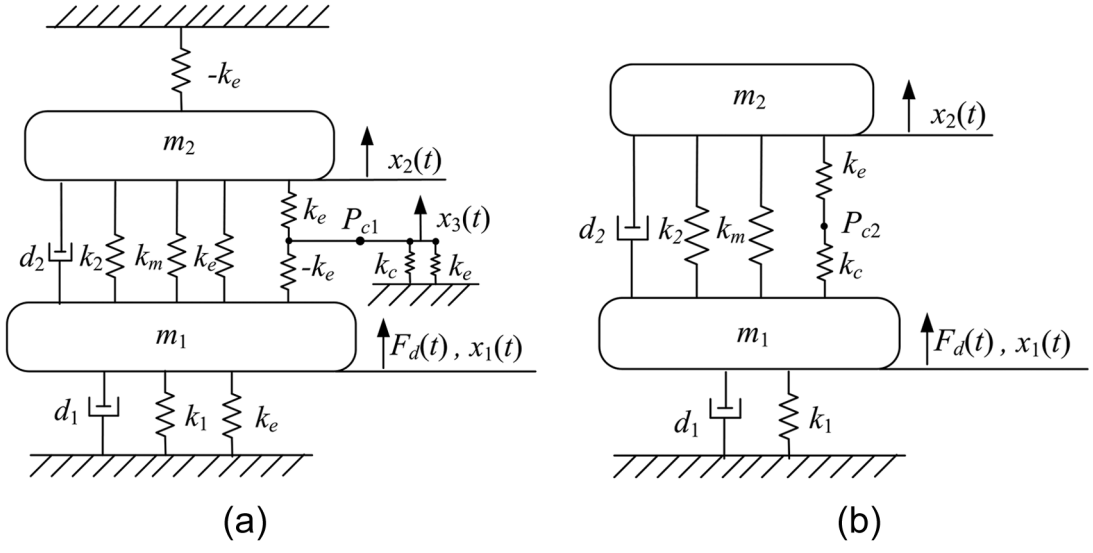


**Figure 3.** Mechanical replacement model for *C* circuit: (a) original model and (b) simplified model.

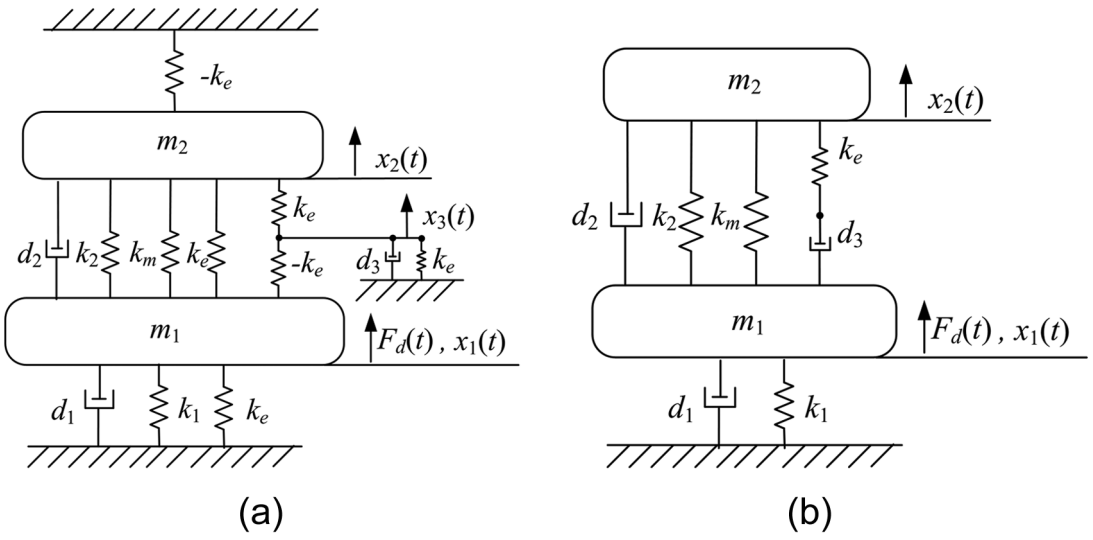


**Figure 4.** Mechanical replacement model for *R* circuit: (a) original model and (b) simplified model.

where $\omega_1 = \sqrt{k_1/m_1}$ is the resonance frequency of the primary structure and $\omega_2 = \sqrt{(k_2 + k_m)/m_2}$ is the resonance frequency of the vibration absorber when the piezo is short-circuited. The equations of motion with normalised parameters can then be written as

$$\begin{bmatrix} 1 & 0 & 0 \\ 0 & \mu & 0 \\ 0 & 0 & \lambda \end{bmatrix} \begin{bmatrix} x_1'' \\ x_2'' \\ x_3'' \end{bmatrix} + \begin{bmatrix} 2D_1 & 0 & 0 \\ 2D_1 & 0 & 0 \\ 0 & 2D_2 & 0 \\ 0 & 0 & 2D_3 \end{bmatrix} \begin{bmatrix} x_1' \\ x_2' \\ x_3' \end{bmatrix} + \begin{bmatrix} 1 + \mu f^2 + \gamma & -\mu f^2 - \gamma & \gamma \\ -\mu f^2 - \gamma & \mu f^2 + \gamma & -\gamma \\ 1 & -1 & 1 + \delta \end{bmatrix} \begin{bmatrix} x_1 \\ x_2 \\ x_3 \end{bmatrix} = \begin{bmatrix} \tilde{F}_s \\ 0 \\ 0 \end{bmatrix} \tag{10a}$$

with

$$\tilde{F}_s = \frac{F_s}{k_1} \tag{10b}$$

An undamped mechanical system is assumed in order to simplify the mathematical expressions in the following sections. This is done by setting the parameters $d_1$, $d_2$, $D_1$ and $D_2$ equal to 0.

Transforming equation (10a) to the frequency domain, the dimensionless driving point mobility of the primary structure with a general *RLC* circuit can be derived

$$Y_{1,p}^{RLC} = \frac{\begin{pmatrix} \lambda\mu\Omega^5\mathrm{i} - ((1+\delta)\mu + \lambda q)\Omega^3\mathrm{i} \\ + 2D_3\mu\Omega^4 - 2D_3 q\Omega^2 + (f^2\mu + \delta q)\Omega\mathrm{i} \end{pmatrix}}{\begin{pmatrix} -\lambda\mu\Omega^6 + 2D_3\mu\Omega^5\mathrm{i} + ((\delta+1)\mu + \lambda O)\Omega^4 \\ -2D_3 O\Omega^3\mathrm{i} - p\Omega^2 + 2D_3 q\Omega\mathrm{i} + f^2\mu + \delta q \end{pmatrix}} \tag{11}$$

where $p = f^2(1+\delta)\mu^2 + ((\delta+1+\lambda)f^2 + \delta + 1 + \delta\gamma)$, $\mu + \gamma(\delta+\lambda)q = \gamma + f^2\mu$ and $O = \mu q + q + \mu$ are substitutions to shorten the expression, and $\Omega = \omega/\omega_1$ is used to normalise the frequency with respect to the resonance frequency of the primary structure.

## Realisation of a piezo-based TVN

In order to realise a piezo-based TVN, the absorber damping introduced by the shunt circuit should be as low as possible as explained in the previous section. This condition is met by a shunted circuit consisting of only a capacitance or an inductance (no resistance). In practice, there always will be some additional mechanical and electrical damping that cannot be removed from the structure, such that the expressions derived in the following paragraphs are valid if the inherent electrical and mechanical damping is sufficiently small to consider the coupled structure as lightly damped.

### *Realisation of a piezo-based TVN with a capacitance circuit*

The system shunt with only a *C* circuit is considered first. This is done by setting the parameters $\lambda$ and $D_3$ in equation (11) equal to 0. The driving point mobility of the primary structure is then given by

$$Y_{1,\mathrm{p}}^{C} = \frac{\left(-(1+\delta)\mu\Omega^2\mathrm{i} + (\mu f^2 + \mu f^2\delta + \delta\gamma)\right)\Omega\mathrm{i}}{(1+\delta)\mu\Omega^4 - (((1+f^2+\gamma)\delta + f^2 + 1)\mu + f^2(1+\delta)\mu^2 + \delta\gamma)\Omega^2 + f^2(1+\delta)\mu + \delta\gamma} \tag{12}$$

When the parameter $\delta$ is negative (negative capacitance), the system might become unstable. Therefore, a stability analysis is performed by applying the Routh–Hurwitz criterion to the characteristic system equation (Meirovitch, 1990), which is the denominator of equation (12). It is shown that the system is stable if and only if $\delta$ is within the boundaries defined by inequalities (13) and (14)

$$\delta > \delta_{cr1} \tag{13}$$

$$\delta < \delta_{cr2} \tag{14}$$

with $\delta_{cr1} = -1 + (\gamma/(\mu f^2 + \gamma))$ and $\delta_{cr2} = -1$.

Physically, the instability occurs when the total effective stiffness of the PBTVA becomes negative. As shown in Figure 3(b), the effective stiffness of the PBTVA $k_{total}$ can be calculated as

$$k_{total} = k_2 + k_m + \frac{k_e k_c}{k_e + k_c} = k_1 \left( \frac{\delta(\gamma + \mu f^2) + \mu f^2}{1 + \delta} \right) \tag{15}$$

where the range of $\delta$ to keep the effective stiffness $k_{total}$ to be positive is the same as given by inequalities (13) and (14).

The asymptotic stability region derived for the $C$ shunt circuit also holds for other circuits containing a capacitor, that is, $RC$ and $RLC$ circuits, as long as $R$ and $L$ are positive. This is because positive resistors and inductors are represented by dampers and masses in the equivalent mechanical model and those elements pose no stability problems.

The driving point mobility of the primary structure given by equation (12) yields two poles and one zero for any $\delta$ within the stable region. The zero $\Omega_z$ is given by

$$\Omega_z = \pm \frac{\sqrt{\mu(1 + \delta)(\gamma\delta + \mu f^2 + \delta\mu f^2)}}{\mu(1 + \delta)} \tag{16}$$

where the sign $\pm$ is used to guarantee that the dimensionless frequency $\Omega_z$ is positive (' + ' is for the stable region given by equation (13) and '−' is for the region defined in equation (14)).

For a harmonic disturbance, effective vibration control of the primary structure is achieved when $\Omega_z$ coincides with the excitation frequency. It is seen that $\Omega_z$ is in function of four parameters: the mass ratio $\mu$, the resonance frequency ratio $f$, the dimensionless electromechanical coupling factor $\gamma$ and the capacitance ratio $\delta$. The first three parameters $f$, $\mu$ and $\gamma$ are related to the system properties and therefore are fixed. Hence, $\delta$ is tuned in order to track a variable excitation frequency. The dependence of the capacitance ratio $\delta$ on the desired zero of the driving point mobility is given by

$$\delta = \frac{\mu(\Omega_z^2 - f^2)}{\gamma - \mu\Omega_z^2 + f^2\mu} \tag{17}$$

The potential of using the $C$ circuit for realising a piezo-based TVN is illustrated on a case study where $\mu$, $f$ and $\gamma$ are set to 0.12, 7.48 and 0.57, respectively. These parameters are obtained based on a finite element analysis of a piezo-based inertial shaker developed in Zhao et al. (2012). Figure 5 plots the primary structure driving point mobility for five different capacitance ratios: $\infty$, 0, −0.922, −0.921 and −0.917. The values 0 and $\infty$ of the capacitance ratio $\delta$ correspond to the piezoelectric element being short-circuited or left open. The remaining capacitance ratios −0.922, −0.921 and −0.917 are chosen such that the zero $\Omega_z$ in equation (17) is located at dimensionless frequencies of 0.5, 1 and 2, respectively. It can be seen in Figure 5 that the response of the primary structure is completely attenuated at the zero of the driving point mobility of the primary structure. In practice, the attenuation will be smaller as some damping, either mechanical or electrical, will always be present in the coupled system. Figure 5 also illustrates that $\Omega_z$ can be tuned by changing the value of the capacitance shunt. The zero response for the open-circuit case occurs at a frequency higher than that for the short-circuit case; this is due to the fact that the piezoelectric element in the PBTVA is stiffer with open electrodes than when they are short connected. As explained in section 'Dynamic analysis of a piezo-based vibration absorber', the piezoelectric element is modelled as two parallel springs $k_m$ and $k_e$ for the open-circuit case, whereas for the short-circuit case only one spring $k_m$ exists.

The results obtained with negative values of the shunt capacitance should be taken with care, since a perfect negative capacitance is assumed, whereas in practice the shunt circuit emulating the negative capacitance exhibits much more complex dynamics, which may preclude the implementation of very large bandwidth of the negative capacitance (De Marneffe, 2007). It is nevertheless useful to have the idealised model described here as a benchmark case.

### *Realisation of a piezo-based TVN with an inductance circuit*

An alternative approach to realise a piezo-based TVN is to connect a shunt circuit including only an inductance to the electrodes of the piezoelectric element of the PBTVA. In that case, the driving point mobility of the primary structure can be derived by setting the parameters $\delta$ and $D_3$ in equation (11) to 0, such that the driving point mobility reads

$$Y_{1,p}^{L} = \frac{-i\Omega\left(\lambda\mu\Omega^4 - (\mu + \lambda\gamma + f^2\lambda\mu)\Omega^2 + f^2\mu\right)}{\lambda\mu\Omega^6 - (f^2\lambda\mu^2 + (1 + (1 + f^2 + \gamma)\lambda)\mu + \lambda\gamma)\Omega^4 + (f^2\mu^2 + (f^2 + f^2\lambda + 1)\mu + \lambda\gamma)\Omega^2 - f^2\mu} \tag{18}$$

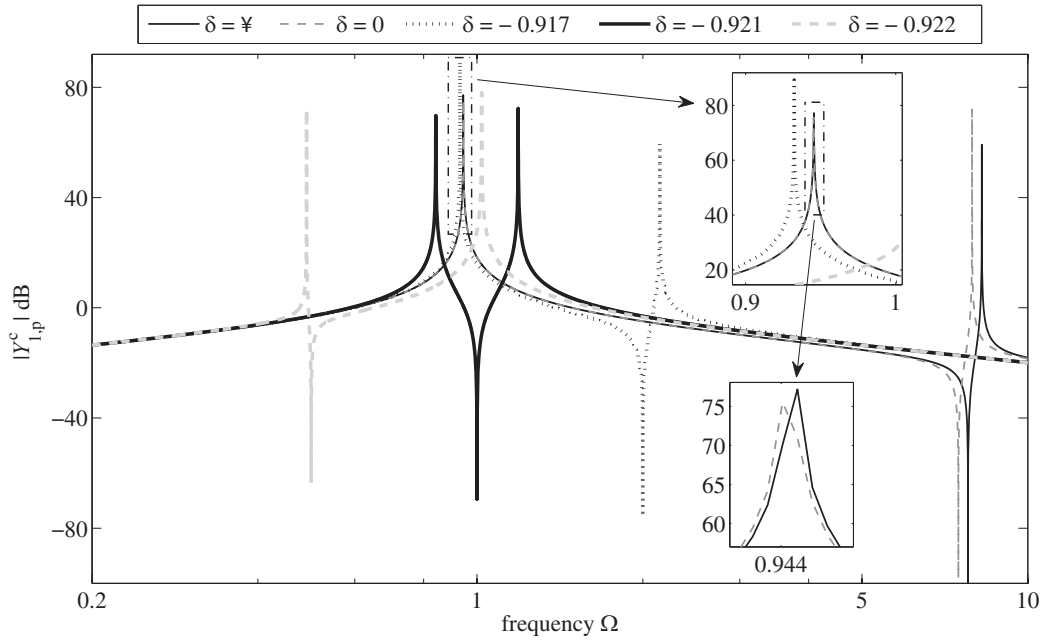


**Figure 5.** Driving point mobility of the primary structure connected to the PBTVA shunt with different capacitances.
PBTVA: piezo-based tuned vibration absorber.

Since the parameter $\lambda$ is presumed to be positive (a positive inductance is attached to the piezoelectric element electrodes), a stability analysis for this system is not needed. The absorbing frequency (the zero of the primary structure driving point mobility) of this system can be obtained by setting the numerator of equation (18) to 0, which yields two solutions

$$\Omega_{z1,z2} = \frac{\sqrt{2}\sqrt{(\gamma + \mu f^2)\lambda + \mu \pm \sqrt{(\gamma + \mu f^2)^2\lambda^2 + (2\gamma\mu - 2\mu^2 f^2)\lambda + \mu^2}}}{2\sqrt{\lambda\mu}} \tag{19}$$

Two absorbing frequencies $\Omega_{z1}$ and $\Omega_{z2}$ (assuming $\Omega_{z1} > \Omega_{z2}$) exist because that there are actually two masses $m_2$ and $m_3$ attached to the primary structure for the $L$ circuit case, and each of them introduces a zero on the driving point mobility of the primary structure. Mass $m_3$ is a virtual mass, delivered to the system by the external inductance, as shown in Figure 2. In contrast to the $C$ shunt circuit case, the parameter $\lambda$ is now used to tune the absorbing frequency to track the variation in the excitation frequency. In order to tune one of the neutraliser absorbing frequencies given by equation (19) to an excitation frequency $\Omega_e$, the parameter $\lambda$ should be tuned to the following value

$$\lambda = \frac{\mu\left(f^2 - \Omega_e^2\right)}{\Omega_e^2\left(-\mu\Omega_e^2 + \gamma + f^2\mu\right)} \tag{20}$$

For positive values of $\lambda$, vibration attenuation can only be obtained when the disturbance frequency is outside the following frequency band given by

$$\Omega_{e1} < \Omega_e < \Omega_{e2} \tag{21}$$

where $\Omega_{e1} = f$ and $\Omega_{e2} = \sqrt{f^2 + \gamma/\mu}$ are the normalised natural frequencies of the PBTVA when the piezoelectric element short- and open-circuited, respectively. The zero of the input driving mobility with the frequency $\Omega_{z2}$ can be used to realise attenuation in the frequency range between 0 and $\Omega_{e1}$, and the other zero $\Omega_{z1}$ in the frequency range between $\Omega_{e2}$ and $\infty$.

The effects of using an $L$ circuit for realising a piezo-based TVN are illustrated in the same example system used in the previous subsection. Figure 6 shows the primary structure driving point mobility plotted against frequency for three different parameters $\lambda$: 3.688, 0.921 and 0.229, which are chosen such that the zero $\Omega_{z2}$ in equation (17) is located at 0.5, 1 and 2, respectively.

It can be seen in Figure 6 that each absorbing frequency (a zero response frequency in the driving point mobility of the primary structure) has an adjacent resonance (pole), which is very close in frequency to the absorbing frequency itself. The adjacent poles and

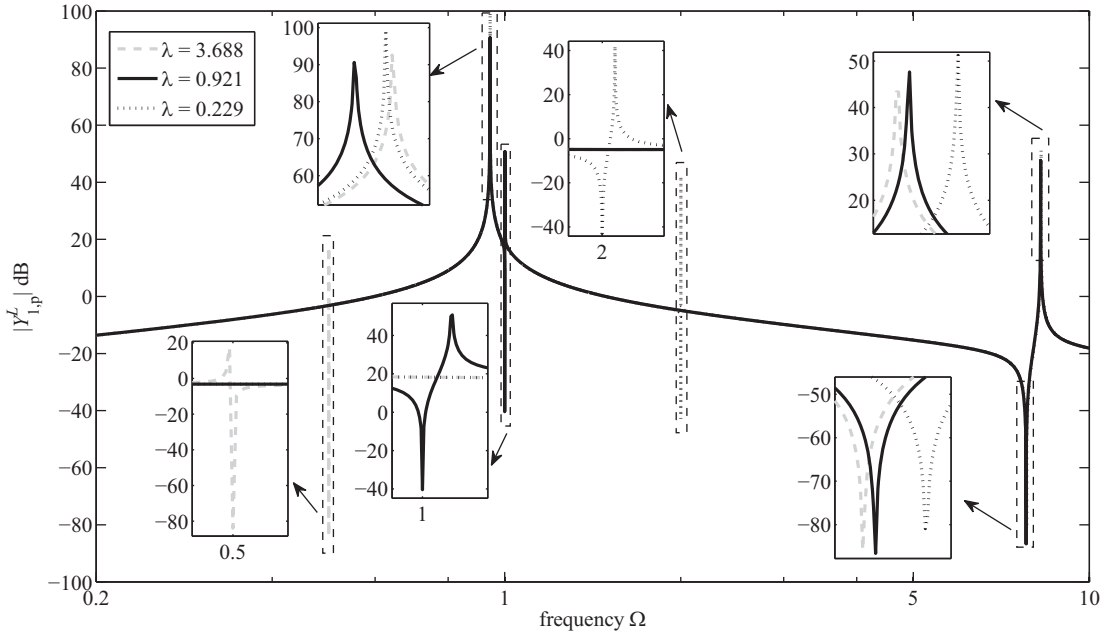


**Figure 6.** Driving point mobility of the primary structure connected to the PBTVA shunt with different inductances.
PBTVA: piezo-based tuned vibration absorber.

zeroes are in fact relatively much closer to each other than in case with the $C$ shunt circuit. This is a limitation in practice, since it will be very difficult to accurately tune the neutraliser. A very small error in tuning could result in the excitation frequency coinciding with the adjacent pole, resulting in a significant increase in vibrations.

Comparing Figures 5 and 6, one can conclude that either an inductance or a capacitance can be connected to a PBTVA to realise a piezo-based TVN, and the effect is similar in both cases since reduction is achieved at one harmonic frequency. However, the $L$ circuit case requires a precise tuning of the shunt inductance due to the vicinity of poles and zeroes, whereas the $C$ shunt case requires a special active electrical circuit to emulate the negative capacitance.

In order to understand the action of an $L$ shunted PBTVA, the deflection shapes of the system corresponding to the three resonance frequencies are shown in Figure 7. At the first resonance, the motion of all three masses is in phase, while at the third resonance, the motion of mass $m_1$ is in phase with the motion of mass $m_3$ and out of phase with the motion of $m_2$. Depending on whether the second normalised resonance frequency is greater than 1, the deflection shape at this pole is different. When it is smaller than 1, mass $m_1$ moves in phase with mass $m_2$ and out of phase with mass $m_3$. If it is larger than 1, the motion of mass $m_1$ is out of phase with the motion of masses $m_2$ and $m_3$. This observation also indicates physically that the proof mass $m_2$ of the PBTVA does not vibrate at all when the second resonance is equal to 1, while the responsiveness of masses $m_1$ and $m_3$ go to $\infty$ at this frequency (Appendix 3). In practice, mechanical damping or electrical resistance, which is always present in the system, will preclude the unbounded response of the masses.

## Realisation of a piezo-based TMD

If the excitation has a broad frequency range, a neutraliser as presented in the previous paragraphs is no longer useful, since amplifications will occur at the new resonances induced by the vibration neutraliser. To avoid this, the PBTVA should be configured as a piezo-based TMD minimising some vibration metrics in the frequency band of interest. For this purpose, certain damping has to be introduced in the suspension of the PBTVA. This can be done by adding a resistor in the shunt circuit, thereby optimally configuring $RL$ and $RC$ circuits are performed in this section.

### *Derivation of the $\mathcal{H}_2$ optimal parameters – minimisation of the kinetic energy*

In this subsection, the kinetic energy of the primary structure is used as the vibration metric to determine the optimal parameters of a PBTVA shunt with $RC$ and $RL$ circuits. A new dimensionless parameter $I_k$ is introduced, which is defined as the ratio of the kinetic energy of the primary system to the excitation force

with a uniform spectrum density $S_f(\omega)$ (Zilletti et al., 2012)

$$I_k = \frac{m_1 E[|v_1|^2]}{2S_f\omega_1/k_1} \tag{22}$$

where $E[]$ denotes the expectation value and $v_1$ is the velocity of the primary mass $m_1$. The unit of $S_f(\omega)$ is $N^2$ s/rad. The constant $S_f\omega_1/k_1$ is introduced to ensure that the performance index is dimensionless. The mean squared value of the velocity of the primary mass can be written as

$$E[|v_1|^2] = \frac{S_f\omega_1}{m_1k_1}\int_{-\infty}^{+\infty}\left|Y_{1,p}\right|^2 \mathrm{d}\Omega \tag{23}$$

where $Y_{1,p}$ is the dimensionless driving point mobility of the primary system.

Substituting equation (23) into equation (22) yields

$$I_k = \frac{1}{2}\int_{-\infty}^{+\infty}\left|Y_{1,p}\right|^2 \mathrm{d}\Omega \tag{24}$$

The derived expression for $I_k$ represents the kinetic energy of the primary mass excited by a white noise spectrum of unit amplitude. The driving point mobility functions of the primary structure for the *RC* and *RL* circuits are derived by setting the parameters $\delta$ for the *RL* circuit and $\lambda$ for the *RC* circuit in equation (11) equal to 0, yielding the following equations

$$Y_{1,p}^{RL} = \frac{\lambda\mu\Omega^5\mathrm{i} + 2D_3\mu\Omega^4 - (\mu+\lambda q)\Omega^3\mathrm{i} - 2D_3q\Omega^2 + f^2\mu\Omega\mathrm{i}}{\begin{pmatrix}-\lambda\mu\Omega^6 + 2D_3\mu\Omega^5\mathrm{i} + (q\lambda\mu + (1+\lambda)\mu + \lambda q)\Omega^4 - 2(q\mu+\mu+q)D_3\Omega^3\mathrm{i}\\ -(f^2\mu^2 + \mu f^2 + \mu + \lambda q)\Omega^2 + 2D_3q\Omega\mathrm{i} + f^2\mu\end{pmatrix}} \tag{25}$$

$$Y_{1,p}^{RC} = \frac{2D_3\mu\Omega^4 - \mu(1+\delta)\Omega^3\mathrm{i} - 2D_3(f^2\mu+\gamma)\Omega^2 + (f^2(1+\delta)\mu + \delta\gamma)\Omega\mathrm{i}}{\begin{pmatrix}2D_3\mu\Omega^5\mathrm{i} + \mu(1+\delta)\Omega^4 - 2D_3(\mu+q\mu+q)\Omega^3\mathrm{i}\\ -(p\mu^2 + (p+1+(1+\gamma)\delta)\mu + \delta\gamma)\Omega^2 + 2qD_3\Omega\mathrm{i} + p\mu + \delta\gamma\end{pmatrix}} \tag{26}$$

where $q = \gamma + f^2\mu$ and $p = f^2(1+\delta)$ are substitutions to shorten the expression.

The performance indices $I_k^{RL}$ and $I_k^{RC}$ for the two shunt circuits can be calculated by substituting the coefficient multiplying powers of $\Omega$ into the integration formulas given in Newland (2012) and James et al. (1947)

$$I_k^{RL} = \frac{\begin{pmatrix}-1/4f^2\begin{pmatrix}(f^2-2r-2)\lambda^2\\ +2\lambda - 4{D_3}^2 - f^2\end{pmatrix}\mu^3 + 2r\begin{pmatrix}(-1/8\gamma - 1/4 + 1/4f^2)\lambda^2\\ +(-1/4f^2+1/4)\lambda - {D_3}^2 + f^2{D_3}^2\end{pmatrix}\mu\\ +\left(1/4\lambda^2 + {D_3}^2\right)\gamma^2 + 1/4f^4\lambda^2\mu^4\\ +\begin{pmatrix}1/4(-\gamma + f^2 - 1)^2\lambda^2 + (f^2 - 1/4\gamma - 1/2f^4 - 1/2)\lambda + \left(1/4 + {D_3}^2\right)f^4\\ +\left(-1/2 - 2{D_3}^2\right)f^2 + {D_3}^2\gamma + {D_3}^2 + 1/4\end{pmatrix}\mu^2\end{pmatrix}2\pi}{D_3\mu^2\gamma} \tag{27}$$

$$I_k^{RC} = \frac{\begin{pmatrix}f^2\mu^3\left((\delta+1)^2f^2 + 4{D_3}^2\right)/4 + 2\gamma\mu\begin{pmatrix}\left(\delta/4 + {D_3}^2 + \delta^2/4\right)f^2\\ +(-1/4+\gamma/8)\delta^2 - \delta/4 - {D_3}^2\end{pmatrix}\\ +\begin{pmatrix}\left(\delta/2 + \delta^2/4 + {D_3}^2 + 1/4\right)f^4 +\\ \left((-1/2+1/2\gamma)\delta^2 + (-1+1/2\gamma)\delta - 2{D_3}^2 - 1/2\right)f^2\\ +1/4 + 1/2\delta + {D_3}^2\gamma + {D_3}^2 + 1/4\delta^2\end{pmatrix}\mu^2 + \gamma^2\left(\frac{\delta^2}{4} + {D_3}^2\right)\end{pmatrix}2\pi}{\mu^2\gamma D_3} \tag{28}$$

For fixed values of $f$, $\mu$ and $\gamma$, the remaining parameters for the optimisation are either $D_3$ and $\lambda$ or $D_3$ and $\delta$ for the *RL* and *RC* circuits, respectively. The optimal parameters $D_{3,\mathrm{opt}}^{RL}$ and $\lambda_{\mathrm{opt}}$, and $D_{3,\mathrm{opt}}^{RC}$ and $\delta_{\mathrm{opt}}$ are found by solving the following equations

$$\begin{cases}\dfrac{\delta I_k^{RL}}{\delta D_3}\left(f,\mu,r,D_{3,\mathrm{opt}}^{RL},\lambda_{\mathrm{opt}}\right) = 0\\ \dfrac{\delta I_k^{RL}}{\delta\lambda}\left(f,\mu,r,D_{3,\mathrm{opt}}^{RL},\lambda_{\mathrm{opt}}\right) = 0\end{cases} \tag{29}$$

$$\begin{cases}\dfrac{\delta I_k^{RC}}{\delta D_3}\left(f,\mu,r,D_{3,\mathrm{opt}}^{RL},\delta_{\mathrm{opt}}\right) = 0\\ \dfrac{\delta I_k^{RC}}{\delta\delta}\left(f,\mu,r,D_{3,\mathrm{opt}}^{RL},\delta_{\mathrm{opt}}\right) = 0\end{cases} \tag{30}$$

resulting in

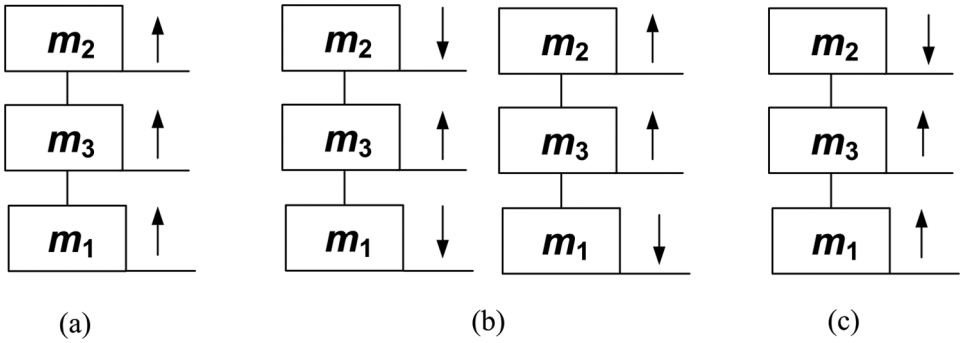


**Figure 7.** Deflection directions of the system using an *L* circuit at (a) the first resonance, (b) the second resonance and (c) the third resonance.

$$D_{3,\mathrm{opt}}^{RL} = \frac{\mu^{3/2}\sqrt{\begin{matrix}\mu^4 f^8 + 2\mu^3 f^6 r + f^2 r(1+f^2 r - 2f^2)\mu^2 \\ + r((-2f^2+3/4)r + 1 - 2f^2 + f^4)\mu + f^2 r^2\end{matrix}}}{2\sqrt{\begin{pmatrix} f^2\mu^3 + (r+1-2f^2+f^4)\mu^2 \\ + (-2r+2f^2 r)\mu + r^2 \end{pmatrix}\begin{pmatrix} f^2\mu^3(f^2\mu - 2r + f^2 - 2) + r^2 \\ + (r - f^2 + 1)^2\mu^2 + r\mu(-2 - r + 2f^2) \end{pmatrix}}} \tag{31}$$

$$\lambda_{\mathrm{opt}} = \frac{\mu(f^2\mu^2 + (-2f^2 + 1/2r + f^4 + 1)\mu - r + f^2 r)}{f^4\mu^4 - f^2(-2r + f^2 - 2)\mu^3 + (-r + f^2 - 1)^2\mu^2 + (-2r + 2f^2 r - r^2)\mu + r^2} \tag{32}$$

$$D_{3,\mathrm{opt}}^{RC} = \frac{\mu^{3/2}\gamma}{2\sqrt{\begin{pmatrix} f^2\mu^3 + (1+r-2f^2+f^4)\mu^2 \\ + (-2\gamma + 2f^2\gamma)\mu + \gamma^2 \end{pmatrix}\begin{pmatrix} f^4\mu^3 + (1+f^4+(2\gamma-2)f^2)\mu^2 \\ + (\gamma^2 - 2\gamma + 2f^2\gamma)\mu + \gamma^2 \end{pmatrix}}} \tag{33}$$

$$\delta_{\mathrm{opt}} = -\frac{(\mu^2 f^4 + (1 + f^4 + (\gamma-2)f^2)\mu - \gamma + f^2\gamma)\mu}{f^4\mu^3 + (1+f^4+(2\gamma-2)f^2)\mu^2 + (\gamma^2 - 2\gamma + 2f^2\gamma)\mu + \gamma^2} \tag{34}$$

whereas the performance indices $I_k^{RL}\mathrm{min}$ and $I_k^{RC}\mathrm{min}$ under their optimal settings are

$$I_{k\,\mathrm{min}}^{RL} = \frac{2\pi\sqrt{\begin{matrix}\begin{pmatrix} f^2(\mu^4 f^6 + r^2) + f^2 r\mu^2(2\mu f^4 + 1 + rf^2 - 2f^2) \\ + ((-2f^2+3/4)r + 1 - 2f^2 + f^4)r\mu \end{pmatrix} \\ (f^2\mu^3 + (-2+2f^2)r\mu + r^2 + (-2f^2 + r + 1 + f^4)\mu^2)\end{matrix}}}{\sqrt{\begin{pmatrix} f^4\mu^4 + (2rf^2 - 2r - r^2)\mu + r^2 \\ -f^2\mu^3(f^2 - 2 - 2r) + (-r - 1 + f^2)^2\mu^2 \end{pmatrix}\sqrt{\mu}r}} \tag{35}$$

$$I_{k\,\mathrm{min}}^{RL} = \frac{2\pi\sqrt{f^2\mu^3 + (\gamma + 1 - 2f^2 + f^4)\mu^2 + (-2\gamma + 2f^2\gamma)\mu + \gamma^2}}{\sqrt{\mu(f^4\mu^3 + (1 + f^4 + (-2+2\gamma)f^2)\mu^2 + (-2\gamma + \gamma^2 + 2f^2\gamma)\mu + \gamma^2)}} \tag{36}$$

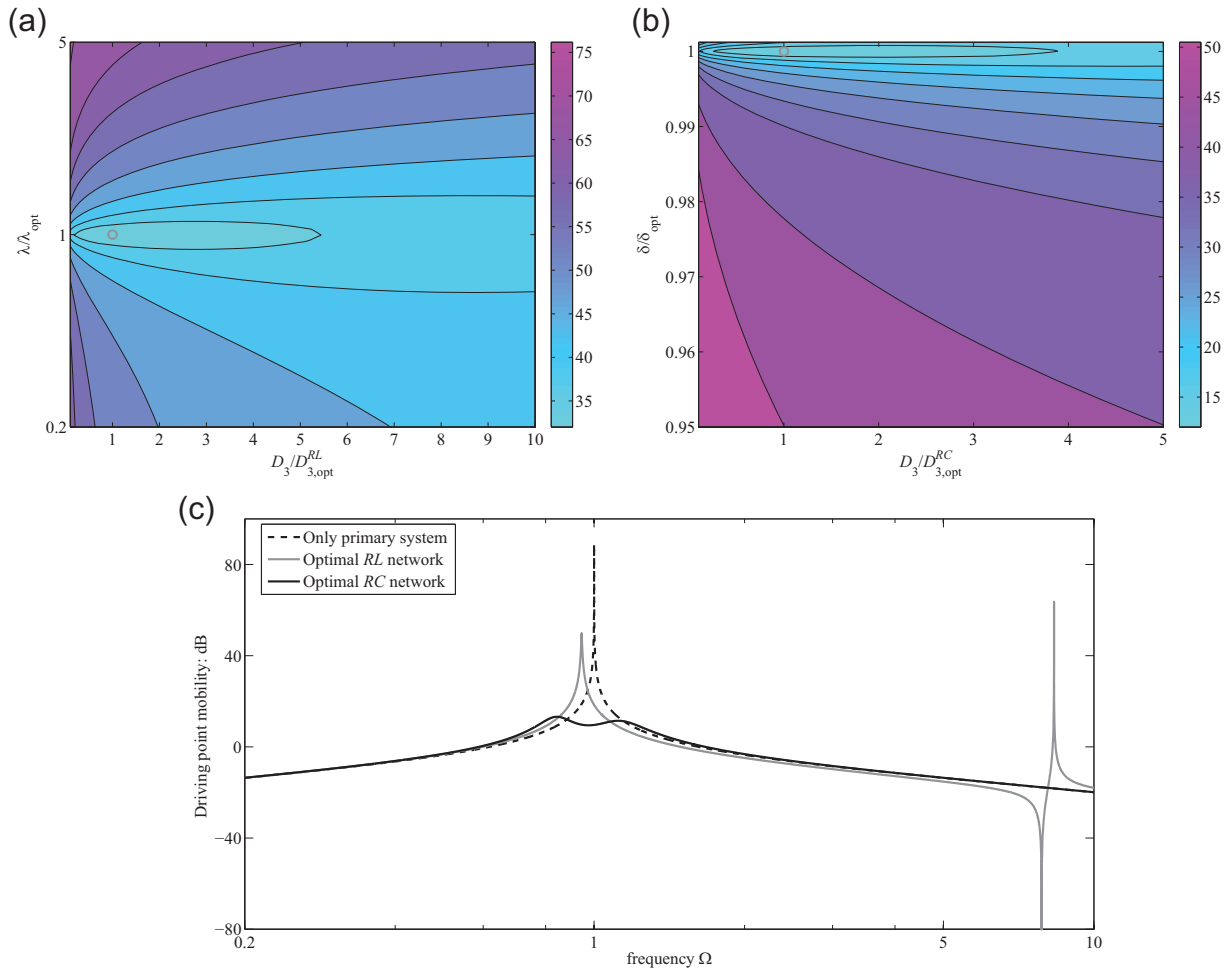


**Figure 8.** (a) Performance index $I_k^{RL}$ against the normalised $D_3$ and $\lambda$, (b) the performance index $I_k^{RC}$ against the normalised $D_3$ and $\lambda$ and (c) the driving point mobility of the primary structure connecting with *RL* and *RC* optimal shunt circuits.

### *Performance comparison*

This subsection compares the performance of the PBTVA shunt with the optimal *RL* and *RC* circuits, respectively. The effects of the two optimal shunt circuits are illustrated on the same example system as discussed earlier in the article. Figure 8(a) and (b) shows the performance index for each shunt circuit plotted against their normalised dependences that are calculated with reference to their optimal values $D^{RL}_{3,\,\mathrm{opt}}$, $\lambda_{\mathrm{opt}}$, $D^{RC}_{3,\,\mathrm{opt}}$ and $\delta_{\mathrm{opt}}$. The optimum (minimum performance index) for each case is marked with a grey circle. Figure 8(c) plots the primary structure driving point mobility against frequency for three different conditions: without the PBTVA being mounted on the primary structure, with the optimally tuned *RL* and *RC* shunted PBTVA on the primary structure. For the optimal *RC* circuit, the resonance of the primary structure is efficiently damped with limited amplification at the two new resonances, while the optimal *RL* shunt circuit tends to give higher steady-state responses around the primary structure resonance frequency and only adds slight damping to the structural mode of the PBTVA. As a consequence, the performance index with the optimally tuned *RC* shunt is about 20 dB better than the *RL* shunt for the considered system. The advantage of using *RC* circuit shunted PBTVA relies on the fact that the *RC* circuit adjusts the effective damping as well as the effective stiffness of the PBTVA so that the proposed system is analogous to the classical TMD. The *RL* circuit shunted PBTVA adds two poles and two zeroes (two absorbers, namely, virtual absorber and physical absorber) to the primary system, where only the virtual absorber can be tuned. For the considered example system, the virtual absorber at the optimal setting is tuned to coincide with the primary structure mode and thus has very little effect to the other mistuned physical mode.

As noted in Figure 8(b), the upper limit of the vertical axis is only slightly greater than 1, which in fact represents the stability limit. This is because the derived optimal capacitance ratio $\delta_{\text{opt}}$ is $-0.9206$ for the considered example system, whereas the stability limit $\delta_{cr1}$ defined in inequality (13) is equal to $-0.9217$. Based on the analogy with the classic TMD, the effective optimal resonance frequency ratio should be slightly lower than 1. Since the initial resonance frequency ratio $f$ of the system for the short connected case is almost 7.5 times larger than 1, a negative value of $\delta$ is thus needed in order to decrease the effective frequency ratio according to equation (15). Therefore, it is useful to analyse some relative stability metrics of the system under the optimal *RC* circuit.

In the following part of the study, the gain margin is used for this purpose. In most cases, the resonance frequency ratio $f$ of the system for the short-circuit case can be expected to be much larger than 1 since the piezoelectric element is very stiff. Therefore, the gain margin between the optimal $\delta_{\text{opt}}$ given in equation (34) and the critical $\delta_{cr1}$ given in inequality (13) as a function of the parameters $f$, $\mu$ and $\gamma$ is studied, which is defined as

$$MAG = \frac{\delta_{cr1}}{\delta_{\text{opt}}} = \frac{(\mu^2 f^4 + (1 + f^4 + (\gamma - 2)f^2)\mu - \gamma + f^2\gamma)(\mu f^2 + \gamma)}{f^2(f^4\mu^3 + (1 + f^4 + (2\gamma - 2)f^2)\mu^2 + (\gamma^2 - 2\gamma + 2f^2\gamma)\mu + \gamma^2)} \tag{37}$$

Figure 9 plots the gain margin against $f$ and $\mu$ for three different values of $\gamma$. It can be seen that the gain margin defined in equation (37) is increased with an increase in $\gamma$ or decrease in $f$ and $\mu$. Nevertheless, this gain margin is relatively small and in most cases is even smaller than 0.2 dB. Therefore, it could thus be argued that the system for the *RC* circuit case is barely stable when the initial resonance frequency ratio $f$ is much larger than 1. On the contrary, if the practical design is such that a short-circuit frequency ratio $f$ is close to unity, then much larger gain margins can be expected. Thus, the design of the mechanical part should be performed with care, using, for example, piezo-transducers with a stroke magnification mechanism, which decreases the short-circuit stiffness of the design. Alternatively, a $d_{31}$ piezoelectric effect could be used in conjunction with bending beam designs, see for example, Alujević et al. (2012). At the moment, a piezostack-based PBTVA is under development for future experimental tests (Zhao et al., 2012).

Besides $\mathcal{H}_2$ optimisation criterion, it is also possible to tune the *RL* using the pole placement method, which seeks to maximise the magnitude of the real part of the system roots. This technique is also referred to as the maximum damping criterion. As pointed out by Preumont (2002), the maximum damping added to a targeted mode by applying *RL* shunt circuit is determined to be half of the generalised modal electromechanical coupling coefficient, which is defined by the ratio of transferred energy and total energy and alternatively calculated as

$$K_i = \sqrt{\frac{\Omega_i^2 - \omega_i^2}{\omega_i^2}} \tag{38}$$

where $i$ represents the $i$th vibration mode of the structure; $\omega_i$ and $\Omega_i$ are the short-circuit and open-circuit resonant frequencies associated with this mode.

For the considered example system, the maximum damping that can be added to the first mode of the

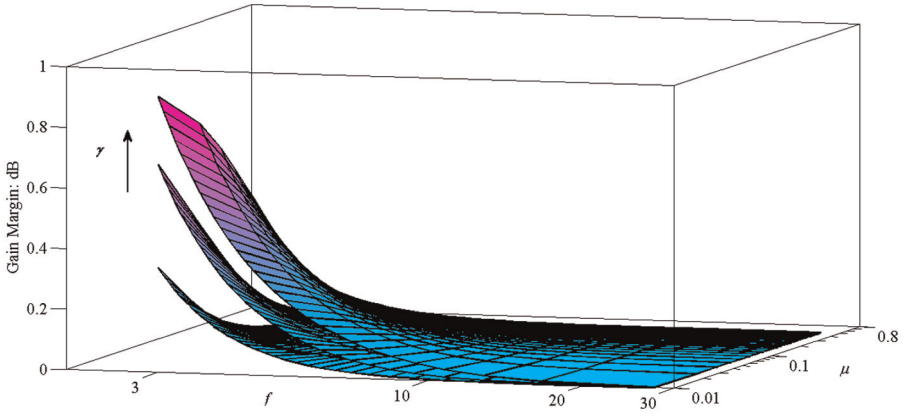


**Figure 9.** Gain margin of the system with the optimal *RC* circuit against $f$, $\mu$ and $\gamma$.

system is calculated as 0.58%, which is almost 3.5 times larger than the damping achieved with the $\mathcal{H}_2$ optimal setting. The difference between the damping achieved with the two criteria is found to be sensitive to the mechanical parameters $f$, $\mu$ and $\gamma$.

The parameter $K_i$ at the primary structure mode is studied, which can be approximated by assuming $f$ is much larger than 1, yielding

$$(K_1)_{f\gg 1} = \frac{\sqrt{\gamma}}{f^2(\mu+1)} + O\left(\frac{1}{f^4}\right) \tag{39}$$

Equation (39) indicates that increasing $\gamma$ and $\mu$ as well as decreasing $f$ will increase the benefit of applying the proposed system in terms of adding more damping to the primary structural mode.

In order to show the similarity between the optimally configured classical TMD and the piezo-based TMD shunt with the optimal *RC* circuit, the performance index for the piezo-based TMD as given in equation (36) is expanded into Taylor series with respect to the inverse value of the resonance frequency ratio $f$, which is again assumed to be much larger than 1

$$\left(I_{k\ \min}^{RC}\right)_{f>1} = \frac{2\pi}{\sqrt{\mu}\sqrt{\mu+1}} + \frac{\pi\sqrt{\mu}(\mu-1)}{(\mu+1)^{3/2}f^2} + O\left(\frac{1}{f^4}\right) \tag{40}$$

If a classical TMD is used to suppress the vibrations of the primary structure, the optimal performance index representing the kinetic energy quantity used in Warburton (1982) takes the form

$$N_{\text{opt}} = \frac{1}{\sqrt{\mu}\sqrt{\mu+1}} \tag{41}$$

where $N$ is defined to be $2\pi$ times smaller than the performance index $I_k$ employed in this article. Apart from this $2\pi$ factor, $N_{\text{opt}}$ is thus the same as the lowest order of the shortened expression given in equation (40). As the higher orders of the Taylor expansion in equation (40) are negative (the mass ratio is assumed to be smaller than 1), this indicates that mounting a perfectly configured PBTVA to a problematic primary structure provides a slightly better vibration reduction than using a classical TMD provided the frequency ratio $f$ is larger than 1. Physically, the reason for this difference is due to the fact that the configurations of the spring and the damper in the two devices are different. For the piezo-based TMD shunt with the *RC* circuit, they can be considered to be placed in series, while the spring and the damper are in parallel for the classical TMD.

## Conclusion

Various shunt circuits are discussed with the intent of realising a piezo-based TVN and a piezo-based TMD in this article. Several equivalent mechanical models of the complete system are derived to better illustrate the coupling of the electrical components with the mechanical systems. The electrical elements resistors, inductors and capacitors are translated as dampers, masses and springs, respectively. It is shown that *C* and *L* circuits can be used to realise a piezo-based TVN, while a piezo-based TMD can be realised by *RC* and *RL* circuits. For the former case, tuning strategies for *C* circuit and *L* circuit are addressed. It is shown that the reduction potential of both circuits is comparable, but there are frequency limits in case of the *L* circuit while there are stability concerns for the *C* circuit when negative capacitances are used.

For the piezo-based TMD, the optimal parameters in the case of *RC* and *RL* circuits have been derived using the $\mathcal{H}_2$ optimisation criterion. The performance of the resulting optimal systems is compared, and it is shown that as expected, the *RC* circuit outperforms the *RL* circuit for a PBTVA in the sense of reducing the kinetic energy of the primary structure. However, one should bear in mind that the gain margin reduces with an increase in the frequency ratio $f$ when the optimal *RC* circuit is connected to the PBTVA. It is also shown that mounting a perfectly configured PBTVA to the problematic primary structure is slightly better than using a classical TMD. This is due to the fact that the equivalent mechanical spring and the damper for the piezo-based TMD case are mounted in series, whereas with classical TMDs they are mounted in parallel.

### Declaration of conflicting interests

The authors declared no potential conflicts of interest with respect to the research, authorship, and/or publication of this article.

### Funding

The author(s) disclosed receipt of the following financial support for the research, authorship, and/or publication of this article: The research of G.Z. was financed by the IWT Flanders within the OptiWind project (GA: IWT/120029) and the China Scholarship Council. The Research Fund KU Leuven is also gratefully acknowledged for its support. The research performed by N.A. was supported financially through an EU FP7 Marie Curie Industry-Academia Partnerships and Pathways (IAPP) Grant Agreement 251211.

### References

Alujević N, Tomac I and Gardonio P (2012) Tuneable vibration absorber using acceleration and displacement feedback. *Journal of Sound and Vibration* 331(12): 2713–2728.

Behrens S, Fleming AJ and Moheimani SOR (2003) A broadband controller for shunt piezoelectric damping of structural vibration. *Smart Materials and Structures* 14: 18–28.

Bonello P, Brennan MJ and Elliott SJ (2005) Vibration control using an adaptive tuned vibration absorber with a

variable curvature stiffness element. *Smart Materials and Structures* 14: 1055–1065.
Corr LR and Clark WW (2001) Energy dissipation analysis of piezoceramic semi-active vibration control. *Journal of Intelligent Material Systems and Structures* 12: 729–736.
Date M, Kutani M and Sakai S (2000) Electrically controlled elasticity utilizing piezoelectric coupling. *Journal of Applied Physics* 87: 863–868.
Davis C and Lesieutre G (2000) An actively tuned solid-state vibration absorber using capacitive shunting of piezoelectric stiffness. *Journal of Sound and Vibration* 232: 601–617.
De Marneffe B (2007) *Active and passive vibration isolation and damping via shunted transducers*. PhD Thesis, Université Libre de Bruxelles, Brussel.
Den Hartog JP (1934) *Mechanical Vibrations*. New York: McGraw-Hill.
Gardonio P and Zilletti M (2013) Integrated tuned vibration absorbers: a theoretical study. *Journal of the Acoustical Society of America* 134: 3631–3644.
Guyomar D, Richard C and Mohammadi S (2008) Damping behavior of semi-passive vibration control using shunt piezoelectric materials. *Journal of Intelligent Material Systems and Structures* 19: 977–985.
Hagood NW and Von Flotow A (1991) Damping of structural vibrations with piezoelectric materials and passive electrical networks. *Journal of Sound and Vibration* 146(2): 243–268.
Hollkamp JJ (1994) Multimodal passive vibration suppression with piezoelectric materials and resonant shunts. *Journal of Intelligent Material Systems and Structures* 5: 49–57.
Hollkamp JJ and Starchville TF (1994) A self-tuning piezoelectric vibration absorber. *Journal of Intelligent Material Systems and Structures* 5: 559–566.
Hunt JB (1979) *Dynamic Vibration Absorbers*. London: Mechanical Engineering Publications Ltd.
Jalili N and Fallahi B (2002) Design and dynamic analysis of an adjustable inertia absorber for semiactive structural vibration attenuation. *Journal of Engineering Mechanics* 128(12): 1342–1348.
James HM, Nicholas NB and Phillips RS (1947) *Theory of Servomechanisms*. McGraw-Hill: New York.
Kidner MRF and Brennan MJ (2001) Varying the stiffness of a beam-like neutralizer under fuzzy logic control. *Journal of Vibration and Acoustics* 124(1): 90–99.
Lesieutre GA (1998) Vibration damping and control using shunted piezoelectric materials. *The Shock and Vibration Digest* 30: 187–195.
Mead DJ (1999) *Passive Vibration Control*. New York: Wiley.
Meirovitch L (1990) *Dynamics and Control of Structures*. New York: Wiley Interscience.
Moheimani SOR and Fleming AJ (2006) *Piezoelectric Transducers for Vibration Control and Damping*. London: Springer.
Neubauer M and Wallaschek J (2010) Efficient modeling of the damping performance of piezoelectric switching techniques using harmonic balance method. In: *Conference on motion and vibration control*, Tokyo, Japan, August, no. 10–203. Institute of Industrial Science, University of Tokyo (Tokyo, Japan).
Neubauer M, Oleskiewicz R, Popp K, et al. (2006) Optimization of damping and absorbing performance of shunted piezo elements utilizing negative capacitance. *Journal of Sound and Vibration* 298: 84–107.
Newland DE (2012) *An Introduction to Random Vibrations, Spectral & Wavelet Analysis*. 3rd ed.New York: Dover Publications Inc.
Niederberger D (2005) *Smart damping materials using shunt control*. PhD Thesis, Swiss Federal Institute of Technology, ETH Zurich, Zurich.
Park CH and Inman DJ (2003) Enhanced piezoelectric shunt design. *The Shock and Vibration Digest* 10: 127–133.
Preumont A (2002) *Vibration Control of Active Structures*. London: Kluwer Academic.
Rustighi E, Brennan MJ and Mace BR (2005) A shape memory alloy adaptive tuned vibration absorber: design and implementation. *Smart Materials and Structures* 14(1): 19–28.
Sales TP, Rade DA and de Souza LCG (2013) Passive vibration control of flexible spacecraft using shunted piezoelectric transducers. *Aerospace Science and Technology* 29: 403–412.
Sun J, Jolly M and Norris M (1995) Passive, adaptive and active tuned vibration absorbers – a survey. *Journal of Mechanical Design* 117(B): 234–242.
Von Flotow AH, Beard A and Bailey D (1994) Adaptive tuned vibration absorbers: tuning laws, tracking agility, sizing and physical implementations. In: *Noise-con 94*, Fort Lauderdale, FL, 1–4 May, pp. 437–454. Noise Control Foundation, New York.
Walsh P and Lamancusa J (1992) A variable stiffness vibration absorber for minimization of transient vibrations. *Journal of Sound and Vibration* 158: 195–211.
Warburton G (1982) Optimum absorber parameters for various combinations of response and excitation parameters. *Earthquake Engineering & Structural Dynamics* 10: 381–401.
Williams K, Chiu G and Bernhard R (2002) Adaptive-passive absorbers using shape-memory alloys. *Journal of Sound and Vibration* 249(5): 835–848.
Wu S (1996) Piezoelectric shunts with parallel R-L circuit of structural damping and vibration control. In: *Society of photo-optical instrumentation engineers (SPIE)*, San Diego, CA, 25 February, vol. 2720, pp. 259–269. Bellingham, WA: SPIE.
Zhao G, Pinte G, Devos S, et al. (2012) A piezo-based rotational inertia shaker for the active control of rotating machinery. In: *International conference on noise and vibration engineering ISMA 2012*, Leuven, 17–19 September, pp. 449–462. Department of Mechanical Engineering, KU Leuven.
Zilletti M, Elliott SJ and Rustighi E (2012) Optimisation of dynamic vibration absorbers to minimise kinetic energy and maximise internal power dissipation. *Journal of Sound and Vibration* 331(18): 4093–4100.

## Appendix 1

### Notation

| | |
|---|---|
| $C$ | capacitor |
| $L$ | inductor |
| $R$ | resistor |

## Appendix 2

In this appendix to the article, it is shown that the models sketched in Figure 3(a) and (b) are equivalent. To

prove the statement, the similarity of the motion equations for $m_1$ and $m_2$ in the two models is compared. For the model shown in Figure 3(a), the equations of motion can be written as

$$m_1\ddot{x}_1 + d_1\dot{x}_1 + d_2(\dot{x}_1 - \dot{x}_2) + k_1x_1 + k_2(x_1 - x_2) - k_m(x_1 - x_2) - k_e(x_3 - x_2 + x_1) = F_s \quad (42)$$

$$m_2\ddot{x}_2 - d_2(\dot{x}_1 - \dot{x}_2) - k_2(x_1 - x_2) + k_m(x_1 - x_2) + k_e(x_3 - x_2 + x_1) = 0 \quad (43)$$

It can be foreseen that the motion equations of the model shown in Figure 3(b) will not contain the term $x_3$. Therefore, it should be replaced with other parameters. Applying the condition that the resultant force at the point $P_{c1}$ is equal to 0 yields

$$(k_e + k_c)x_3 + k_e(x_1 - x_2) = 0 \quad (44)$$

which can be rewritten as

$$x_3 = \frac{k_e(x_2 - x_1)}{k_e + k_c} \quad (45)$$

Substituting equation (45) into equations (42) and (43) yields

$$m_1\ddot{x}_1 + d_1\dot{x}_1 + d_2(\dot{x}_1 - \dot{x}_2) + k_1x_1 + k_2(x_1 - x_2) - k_m(x_1 - x_2) - \frac{k_ek_c}{k_e + k_c}(x_1 - x_2) = F_s \quad (46)$$

$$m_2\ddot{x}_2 - d_2(\dot{x}_1 - \dot{x}_2) - k_2(x_1 - x_2) + k_m(x_1 - x_2) + \frac{k_ek_c}{k_e + k_c}(x_1 - x_2) = 0 \quad (47)$$

Let us now write down the motion equations for the model shown in Figure 3(b). Before proceeding to the equations, it is noted that two springs of series connection can be grouped into one equivalent spring to simplify the analysis. For the case in Figure 3(b), springs $k_c$ and $k_e$ can be represented by a new spring connected between masses $m_1$ and $m_2$, which takes the form

$$k_{\text{equivalent}} = \frac{k_ek_c}{k_e + k_c} \quad (48)$$

Now it is easy to derive the equations of motion for the model sketched in Figure 3(b), which can be written as

$$m_1\ddot{x}_1 + d_1\dot{x}_1 + d_2(\dot{x}_1 - \dot{x}_2) + k_1x_1 + k_2(x_1 - x_2) - k_m(x_1 - x_2) - \frac{k_ek_c}{k_e + k_c}(x_1 - x_2) = F_s \quad (49)$$

$$m_2\ddot{x}_2 - d_2(\dot{x}_1 - \dot{x}_2) - k_2(x_1 - x_2) + k_m(x_1 - x_2) + \frac{k_ek_c}{k_e + k_c}(x_1 - x_2) = 0 \quad (50)$$

Comparing equations (46) and (47) with (49) and (50), respectively, it can be proved that the models shown in Figure 3(a) and (b) are equivalent.

## Appendix 3

This appendix studies the deflection shapes of the system at the corresponding resonances where an $L$ circuit is connected to the piezoelectric element. For this purpose, the frequency response functions from the displacements of masses $m_1$, $m_2$ and $m_3$ to the exciting force are first derived, which take the following normalised forms

$$T^L_{1,1} = \frac{\lambda\mu\Omega^2 + (-\mu - \lambda r - f^2\lambda\mu)\Omega + f^2\mu}{Den} \quad (51)$$

$$T^L_{1,2} = \frac{-\lambda(r + f^2\mu)\Omega + f^2\mu}{Den} \quad (52)$$

$$T^L_{1,3} = \frac{\mu\Omega}{Den} \quad (53)$$

with $Den = -\lambda\mu\Omega^3 + (f^2\lambda\mu^2 + \lambda r + (1 + (f^2 + r + 1)\lambda)\mu)\Omega^2 - (-f^2\mu^2 - \lambda r + (-f^2\lambda - f^2 - 1)\mu)\Omega + f^2\mu$ and $\Omega = \omega^2/{\omega_1}^2$.

It can be seen that the considered system is a 3-degree-of-freedom vibrational system without damping. Therefore, it must have three real natural frequencies, namely, $\Omega_{p1}$, $\Omega_{p2}$ and $\Omega_{p3}$, representing the first, second and third resonances, respectively ($\Omega_{p1} < \Omega_{p2} < \Omega_{p3}$). These parameters are obtained as the solutions of the denominator $Den$

$$-\lambda\mu\Omega^3 + \left(f^2\lambda\mu^2 + \lambda r + (1 + (f^2 + r + 1)\lambda)\mu\right)\Omega^2 + \left(-f^2\mu^2 - \lambda r + (-f^2\lambda - f^2 - 1)\mu\right)\Omega + f^2\mu = 0 \quad (54)$$

Considering the numerator of equation (51), it is a quadratic polynomial, which necessarily becomes 0 for two frequencies, namely, $\Omega^{11}_{z1}$ and $\Omega^{11}_{z2}$. In general, we may make the following statement: the three resonance frequencies are separated by the two zeroes of equation (51), which can be better interpreted in inequality (55)

$$\Omega_{p1} < \Omega^{11}_{z1} < \Omega_{p2} < \Omega^{11}_{z2} < \Omega_{p3} \quad (55)$$

Now, we introduce two new functions $f_1$ and $f_2$ to represent the numerators of the equations (51) and (52), respectively, which take the forms

$$f_1(\Omega) = \lambda\mu\Omega^2 + \left(-\mu - \lambda r - f^2\lambda\mu\right)\Omega + f^2\mu \quad (56)$$

$$f_2(\Omega) = -\lambda\left(r + f^2\mu\right)\Omega + f^2\mu \quad (57)$$

As the coefficient of the term $\Omega^2$ in equation (56) is positive, $f_1(\Omega)$ can be proved to be smaller than 0 when the variable $\Omega$ is within the range between $\Omega^{11}_{z1}$ and $\Omega^{11}_{z2}$,

while it is greater than 0 when the variable $\Omega$ is out of this range. Using inequality (55), one can obtain the following inequalities

$$\begin{aligned} f_1(\Omega_{p1}) &> 0 \\ f_1(\Omega_{p2}) &< 0 \\ f_1(\Omega_{p3}) &> 0 \end{aligned} \tag{58}$$

It is seen that the numerator of equation (53) is positive for any given resonance frequency. In addition, the frequency response functions shown in equations (51) to (53) have the same denominator so that the motion directions of the masses at each resonance frequency are only determined by the signs of the numerators. Therefore, it can be concluded that masses $m_1$ and $m_3$ are vibrating in phase at the first and third resonances, while they move out of phase at the second resonance.

In order to better illustrate the motion direction of mass $m_2$ with reference to the other two masses, the denominator *Den* is rearranged as

$$Den = (1-\Omega)f_1(\Omega) - \mu\Omega f_2(\Omega) \tag{59}$$

Considering the expression for $f_2(\Omega)$ in equation (57), it can be seen that $f_2(\Omega)$ is equal to 0 when the conditions $\lambda = f^2\mu/(r+f^2\mu)$ and $\Omega = 1$ are satisfied. The above pair of values is of particular interest since the denominator *Den* as given in equation (59) is also equal to 0, which means mass $m_2$ does not vibrate at all ($f_2(\Omega)$ is equal to 0) at the resonance frequency $\Omega$, which is equal to 1.

Substituting the second resonance $\Omega_{p2}$ into equation (59) yields

$$(1-\Omega_{p2})f_1(\Omega_{p2}) - \mu\Omega_{p2}f_2(\Omega_{p2}) = 0 \tag{60}$$

When $\Omega_{p2}$ is smaller than 1, the first term of left-hand side of equation (60) $(1-\Omega_{p2})f_1(\Omega_{p2})$ turned out to be smaller than 0, which requires the second term $\mu\Omega_{p2}f_2(\Omega_{p2})$ to be smaller than 0 as well. This statement is true because the left-hand side of equation (60) has to be equal to 0. Therefore, $f_2(\Omega_{p2})$ can be derived to be smaller than 0 when the second resonance $\Omega_{p2}$ is smaller than 1. Using a similar procedure, it can be derived that $f_2(\Omega_{p2})$ is greater than 0 when $\Omega_{p2}$ is greater than 1. It can also be stated that $\Omega_{p1}$ should be smaller than 1 and $\Omega_{p3}$ should be greater than 1. Combining this statement with the previous procedure, it can be derived that $f_2(\Omega_{p1})$ is greater than 0 and $f_2(\Omega_{p3})$ is smaller than 0.

In conclusion, at the first resonance, the motion of all the masses is in phase, while at the third resonance, the motion of mass $m_1$ is in phase with the one of mass $m_3$ and out of phase with the one of $m_2$. Depending on whether the second resonance is greater than 1, the mode shape for this pole is different. When it is smaller than 1, mass $m_1$ moves in phase with mass $m_2$ and out of phase with mass $m_3$. If it is larger than 1, the motion of mass $m_1$ is out of phase with the motions of masses $m_2$ and $m_3$.